Supplementary Information

CONTENTS

I. IDENTIFYING SELENIUM ATOMS

Averaged selenium density

The cleaved top-most layer imaged by STM is the chalcogen layer. Since Se is smaller than Te, the apparent height of the STM topographic image at a Se site is expected to be lower than that at a Te site. Based on this difference, we can identify the atomic species at all atomic-lattice sites. This allows us to argue not only the averaged chemical compositions [S1–S3] but also the spatial distribution of the Se atoms.

To execute this analysis, we first acquired a high-resolution (4096×4096 pixels) topographic image in the same FOV investigated in the main text (Fig. S1**a**). We then used the Lawler-Fujita algorithm [S4] to determine the atomic-lattice sites precisely (inset of Fig. S1**a**). Before extracting the apparent height at each atomic-lattice site, we removed long-wavelength background modulations from the original topographic image by high-pass filtering with the cutoff wavelength of 0.67 nm^{-1} (Fig. S1**b**). The histogram of the apparent heights at the atomic-lattice sites in the filtered image exhibits two distinct peaks that can be fitted well by two Gaussian functions (Fig. S1**c**). The lower and higher peaks correspond to the Se and Te sites, respectively. From the areas of the peaks, we estimated the averaged Se density to be 39.7 %, which agrees with the nominal composition.

Identifying selenium and tellurium sites

To separate Se sites from the Te sites, we defined the threshold height at which the two Gaussian functions cross each other as indicated by the arrow in Fig. S1**c**. The atomic-lattice sites with lower and higher apparent heights than the threshold were regarded as the Se and Te sites, respectively. The relevance of this identification procedure is demonstrated in the inset of Fig. S1**b**.

Making local selenium-density map

To investigate the correlation between the local Se density and the vortices with and without the ZVBS, we need to make a Se-density map. We defined the local Se density $D_{\mathrm{Se}}(\mathbf{r})$ as an averaged Se density over a circular area with a diameter d centered at $\mathbf{r}$. Figure S1**d-i** shows examples of $D_{\mathrm{Se}}(\mathbf{r})$ with different d in the same FOV investigated in the main text. As expected, the length scale of the spatial variation of $D_{\mathrm{Se}}(\mathbf{r})$ increases with increasing d, whereas the deviation from the averaged value decreases. Even in the case of the small $d = 8$ nm, which roughly corresponds to the size of the individual vortex, fluctuations in $D_{\mathrm{Se}}(\mathbf{r})$ are less than 10 %.

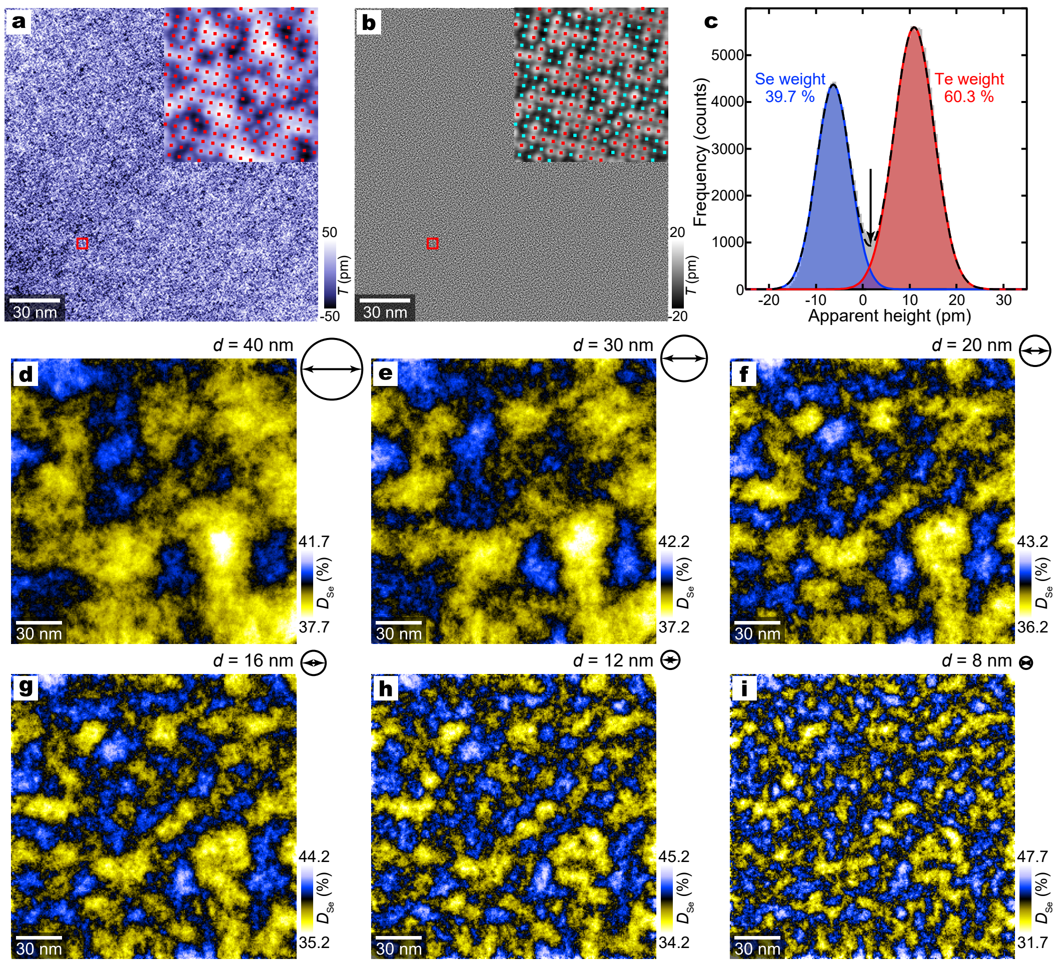

FIG. S1. **Identifying Se and Te sites.** **a**, A high-resolution constant-current topographic image. (Same as Fig. 1**a** in the main text). The inset shows a magnified image of the region marked by the red box. Red dots denote the chalcogen sites determined by the Lawler-Fujita algorithm [S4]. **b**, A high-pass-filtered image of **a**. Blue and red dots in the inset represent the Se and Te sites, respectively. **c**, A histogram of the apparent heights at the all chalcogen sites in the high-pass-filtered image. Black dashed curve represents the fitted results obtained using two Gaussian functions. Blue, and red curves are the individual Gaussian functions of the lower and higher peaks, respectively. A black arrow indicates the threshold value being used to distinguish the Se sites from the Te sites. **d-i**, Se density maps $D_{\mathrm{Se}}(\mathbf{r})$ with the the diameters of circular averaging area of 40, 30, 20, 16, 12, and 8 nm, respectively. The size of the averaging area is indicated by a circle at the right upper corner of each panel.

II. DEFECT IMAGES AT DIFFERENT ENERGIES

We observed many defects characterized by pairs of LDOS peaks appearing at symmetric energies within the superconducting gap $\Delta(\mathbf{r})$, as shown in Fig. 1**b** in the main text. Figure S2**b-f** shows the E dependence of the conductance maps $g(\mathbf{r}, E)$ around one of the defects. Since no topographical signature associated with the defect is observed in the simultaneously acquired topographic image (Fig. S2**a**), it is conceivable that the defect is located underneath the surface. A point like feature appears at $+100$ μeV, as indicated by the arrow in Fig. S2**b**. With increasing E, this feature spreads out in space (Fig. S2**c-f**). A line profile of the tunneling spectra taken along the path through the center of the impurity depicts the spatial evolutions of the impurity bound states clearly (Fig. S2**g**).

We note that the defect-state energy saturates at ~ 0.8 meV that is below $\Delta(\mathbf{r})$. We found that the onset energies above which the defect states become visible vary from defect to defect whereas the upper-bound energies of the defect states are similar for most of the defects. Therefore, the apparent number of defects imaged in $g(\mathbf{r}, E)$ increases with increasing E as shown in Fig. S2**h-j**. A convenient way to map out all of the defects appearing at different energies is to map out $I(\mathbf{r}, E)$ at E slightly lower than $\Delta(\mathbf{r})$, because $I(\mathbf{r}, E)$ reflects the energy-integrated LDOS. Here we use $I(\mathbf{r}, E = 1 \text{ meV})$ for the defect image (Fig. S2**k**)

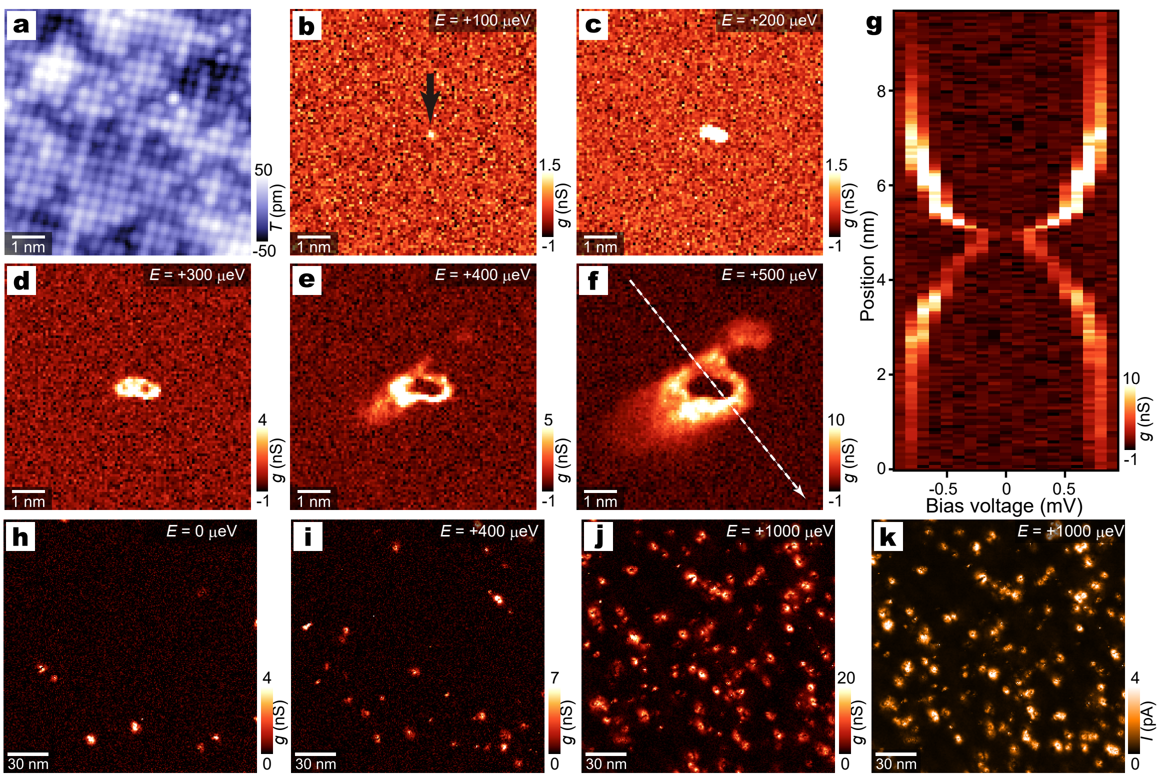

FIG. S2. **Energy dependence of the defect state.** **a**, A topographic image over an 8 nm × 8 nm FOV around a defect. **b-f**, Conductance maps $g(\mathbf{r}, E)$ at $E = +100$, $+200$, $+300$, $+400$, and $+500$ μeV, respectively in the same FOV as **a**. **g**, A line profile of the tunneling spectra along the white dashed arrow in **f**. These images were taken with the setpoint of $I = 100$ pA at $V = -10$ mV and the lock-in modulation was set to $V_{\rm mod} = 70.7$ $\mu V_{\rm rms}$. **h-j**, Conductance maps $g(\mathbf{r}, E)$ at $E = 0$, $+400$, and $+1000$ μeV, respectively, in the same FOV as Fig. 1**a** in the main text. **k**, Current image $I(\mathbf{r}, E = 1 \text{ meV})$ in the same FOV. These images were taken with the setpoint of $I = 100$ pA at $V = -10$ mV and the lock-in modulation was set to $V_{\rm mod} = 141$ $\mu V_{\rm rms}$.

III. MULTIPLE PEAK FITTING OF THE TUNNELING SPECTRA

Tunneling spectra at the vortex centers possess multiple peaks as shown in Fig. 2 in the main text and Fig. S3. To extract the energy, amplitude, and width of each vortex bound state, we fitted the observed spectrum to the fitting function $g_{\text{fit}}(E)$ consisting of multiple Lorentzian functions,

$$g_{\text{fit}}(E) = \sum_{n=1}^{N} \left\{ \frac{A_n w_n^2}{(E - E_n)^2 + w_n^2} \right\}, \tag{S1}$$

where N is the number of peaks in the spectrum. E_n, A_n, and w_n are the energy, amplitude, and width of the n-th peak, respectively. All these quantities except N are used as fitting parameters. Before the fitting, we have to determine N and initial values of E_n, A_n, and w_n. For N, we first calculated the second derivative of each spectrum $-d^2g(\mathbf{r}, E)/dE^2$ to identify the peaks in $g(\mathbf{r}, E)$ clearly. We counted the peak if the peak intensity and the peak sharpness satisfy $g(\mathbf{r}, E_n) > 1$ nS and $-d^2g(\mathbf{r}, E)/dE^2 > 100$ nS/V^2, respectively. The initial values of E_n were set to the energies of these counted peaks. The initial values of A_n were set to $g(\mathbf{r}, E_n)$ and we used the initial value of 50 μeV for w_n of all peaks. We were able to fit most of the spectra reasonably well using this procedure. Nevertheless, in some cases, the fitting results in unreasonable parameters, such as negative A_n and/or w_n, smaller than the experimental energy resolution. In such cases, we removed the peaks with unreasonable parameters from $g_{\text{fit}}(E)$ and performed fitting again until all of the parameters converged to reasonable values. Some of the fitting examples are shown in Fig. S3**a-d**.

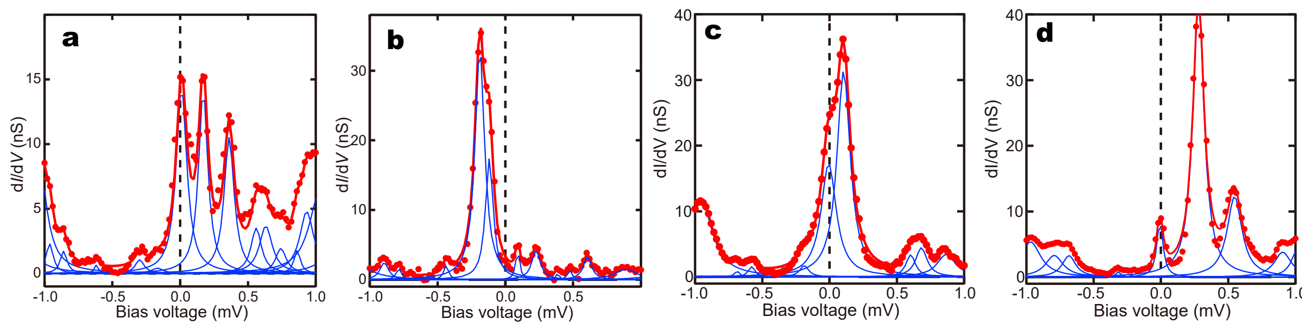

FIG. S3. **Fitting tunneling spectra at representative vortex centers. a-d**, Tunneling spectra at representative vortex centers in $B = 1$ T obtained by numerical differentiation of the I-V curves with sampling interval of 20 μV. The setpoints of the measurements are all $I = 100$ pA at $V = -10$ mV. Red circles and lines show the experimental data and the fitted curves, respectively. Blue lines indicate the decomposed Lorentzian functions.

IV. MAKING LOCAL SUPERCONDUCTING-GAP MAP

We defined the local superconducting gap $\Delta(\mathbf{r})$ as the energy of the highest peak in $g(\mathbf{r}, E)$ on the positive energy side, as indicated by the red arrow in Fig. S4**a**. Figure S4**b** shows the spatial distribution of $\Delta(\mathbf{r})$ in the FOV investigated in the main text. The histogram of $\Delta(\mathbf{r})$ shows that the averaged $\Delta(\mathbf{r})$ is 1.96 meV with the standard deviation of 0.31 meV (Fig. S4**c**).

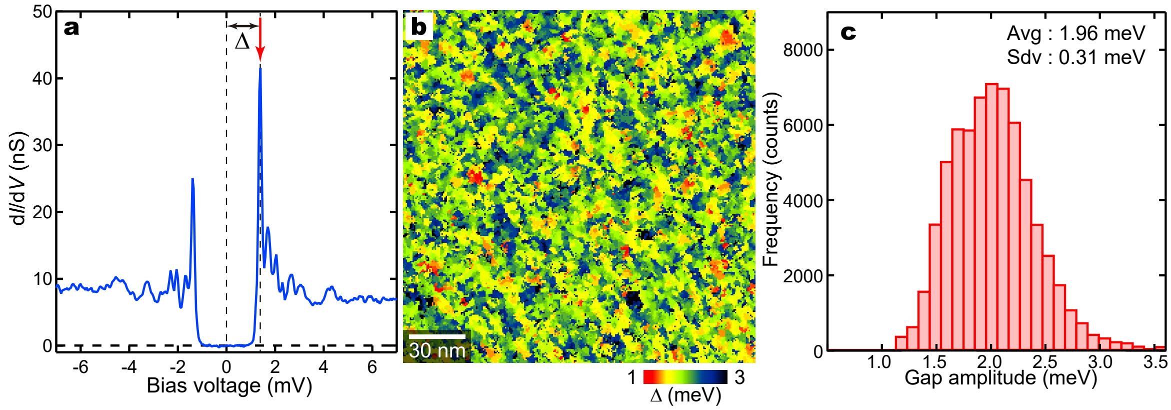

FIG. S4. **Spatial variation of the superconducting gap.** **a**, A typical tunneling spectrum in zero magnetic field. The setpoint was $I = 100$ pA at $V = -10$ meV. The red arrow indicates the defined superconducting-gap energy where the conductance takes a maximum on the positive energy side. **b**, A superconducting gap map $\Delta(\mathbf{r})$ in the same FOV investigated in the main text. **c**, A histogram of $\Delta(\mathbf{r})$.

V. DETAILS OF THE CROSS-CORRELATION ANALYSES

To evaluate the spatial correlation between the vortices with and without the ZVBS and the preexisting quenched disorders quantitatively, we performed cross-correlation analyses. We define a normalized cross-correlation function $C[X(\mathbf{r}); Y(\mathbf{r}), \mathbf{R}]$ between two images $X(\mathbf{r})$ and $Y(\mathbf{r})$ as

$$C[X(\mathbf{r}); Y(\mathbf{r}), \mathbf{R}] = \frac{\int[(X(\mathbf{r}) - \bar{X})(Y(\mathbf{r}+\mathbf{R}) - \bar{Y})]d\mathbf{r}}{\sqrt{A_{X,X}(0)A_{Y,Y}(0)}}, \tag{S2}$$

where the bar denotes the spatially averaged value and $A_{X,X}(\mathbf{R})$ is an auto-correlation defined as

$$A_{X,X}(\mathbf{R}) = \int[(X(\mathbf{r}) - \bar{X})((X(\mathbf{r}+\mathbf{R}) - \bar{X})]d\mathbf{r}. \tag{S3}$$

$C[X(\mathbf{r}); Y(\mathbf{r}), \mathbf{R}]$ represents the similarity between two images with a relative displacement of $\mathbf{R}$ and takes values from +1 (perfect correlation) to -1 (perfect anti-correlation). If $C[X(\mathbf{r}); Y(\mathbf{r}), \mathbf{R}] \sim 0$, the correlation is weak between $X(\mathbf{r})$ and $Y(\mathbf{r}+\mathbf{R})$.

In the present case, $X(\mathbf{r})$ is the vortex image and $Y(\mathbf{r})$ is one of the images of quenched disorders. We adopted a simplified vortex image $V_{\mathrm{All}}(\mathbf{r})$ defined as

$$V_{\mathrm{All}}(\mathbf{r}) = \sum_{i}^{N} \exp\left\{-\frac{1}{2\sigma^2}\left[(x-x_i)^2 + (y-y_i)^2\right]\right\}, \tag{S4}$$

where N, $(x_i,\ y_i)$, and σ are the total number of vortices in the FOV, the coordinate of i-th vortex center, and the width of the Gaussian distribution. We set $(x_i,\ y_i)$ at the locations where $g(\mathbf{r}, E = 0\ \mathrm{meV})$ takes a maximum in individual vortex areas and we set $\sigma = 4$ nm for all vortices to mimic the decay length of the observed bound states. $V_{\mathrm{All}}(\mathbf{r})$ was then separated into two vortex images according to the presence $[V_{\mathrm{Z}}(\mathbf{r})]$ or absence $[V_{\mathrm{N}}(\mathbf{r})]$ of the ZVBS. These vortex images are shown in Fig. S5 for $B = 1$ T and 3 T. In the following, we calculate the azimuthally-averaged normalized cross-correlation functions between these three vortex images and the images of quenched disorders.

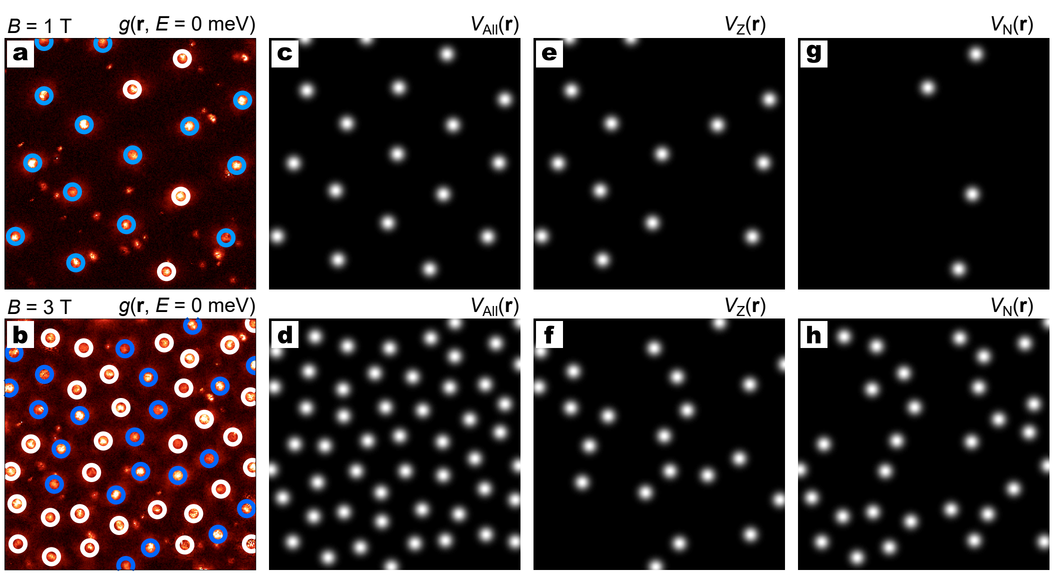

FIG. S5. **Making simplified vortex images.** **a**,**b** Maps of $g(\mathbf{r}, E = 0\ \mathrm{meV})$ at $B = 1$ T and 3 T, respectively, showing vortices. Blue and white circles represent vortices with and without the ZVBS, respectively. **c**,**d** Simplified images of all vortices at $B = 1$ T and 3 T, respectively. **e**,**f** Simplified images of vortices with the ZVBS at $B = 1$ T and 3 T, respectively. **g**,**h** Simplified images of vortices without the ZVBS at $B = 1$ T and 3 T, respectively.

Correlations between vortices and local selenium density

In Fig. S6, we show correlations between vortex images and local Se density $D_{\mathrm{Se}}(\mathbf{r})$. Because $D_{\mathrm{Se}}(\mathbf{r})$ depends on the diameter d of the averaging area, we performed calculations using various d values. In all the cases, the absolute values of the cross-correlation functions are ~ 0.1 at most, suggesting that the chemical disorder is nothing to do with the ZVBS.

In principle, we may need to consider the Se distributions in the subsurface layers as well. Although subsurface layers are invisible to STM, fluctuations should becomes smaller if Se distributions are averaged over multiple layers. Since it is suggested that 50 % Te substitution is enough to make Fe(Se,Te) a topological superconductor [S5–S8] and fluctuations in $D_{\mathrm{Se}}(\mathbf{r})$ are less than 10 % in the top-most layer (Fig. S1), we can safely conclude that there would be little chance to have Se-rich regions without the topological surface state. Therefore, it is unlikely that the presence or absence of the ZVBS is governed by the local Se density.

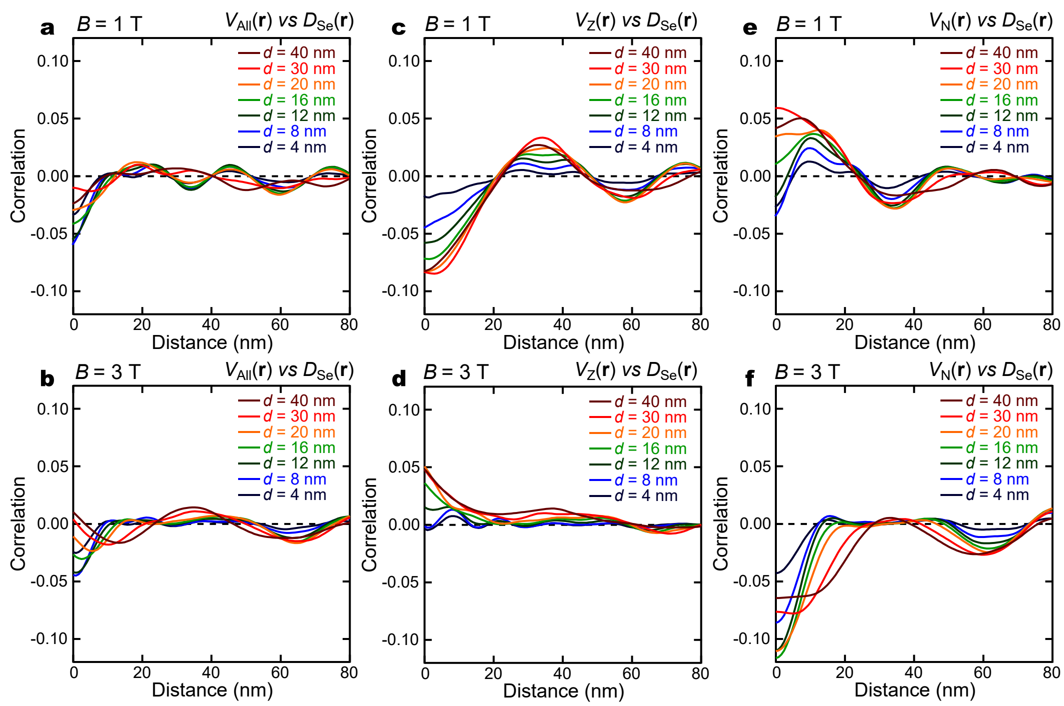

FIG. S6. **Correlation between the vortices and local Se density.** **a**,**b** Azimuthally-averaged cross-correlation functions between all vortices and the local Se density at $B = 1$ T and 3 T, respectively. **c**,**d** Azimuthally-averaged cross-correlation functions between vortices with the ZVBS and the local Se density at $B = 1$ T and 3 T, respectively. **e**,**f** Azimuthally-averaged cross-correlation functions between vortices without the ZVBS and the local Se density at $B = 1$ T and 3 T, respectively. We show results with the different Se-density maps obtained by using the different diameters of circular averaging areas indicated in each panel.

Correlations between vortices and defects

Next we examined the correlations between vortices and $I(\mathbf{r}, E = 1\ \mathrm{meV})$ that represents the defect distribution. Figure S7**a-c** shows the azimuthally-averaged $C[V_{\mathrm{All}}(\mathbf{r}); I(\mathbf{r}, E = 1\ \mathrm{meV}), R]$, $C[V_{\mathrm{Z}}(\mathbf{r}); I(\mathbf{r}, E = 1\ \mathrm{meV}), R]$, and $C[V_{\mathrm{N}}(\mathbf{r}); I(\mathbf{r}, E = 1\ \mathrm{meV}), R]$, respectively. The absolute values of the cross-correlation functions are always less than 0.05. We also investigated the cross-correlation functions between vortex images and the energy-resolved defect images $g(\mathbf{r}, E)$. As shown in Fig. S7**d-f**, $C[V_{\mathrm{All}}(\mathbf{r}); g(\mathbf{r}, E), R = 0]$, $C[V_{\mathrm{Z}}(\mathbf{r}); g(\mathbf{r}, E), R = 0]$, and $C[V_{\mathrm{N}}(\mathbf{r}); g(\mathbf{r}, E), R = 0]$ are again all less than ~ 0.05. From these results, we conclude that the ZVBS and defects are unrelated.

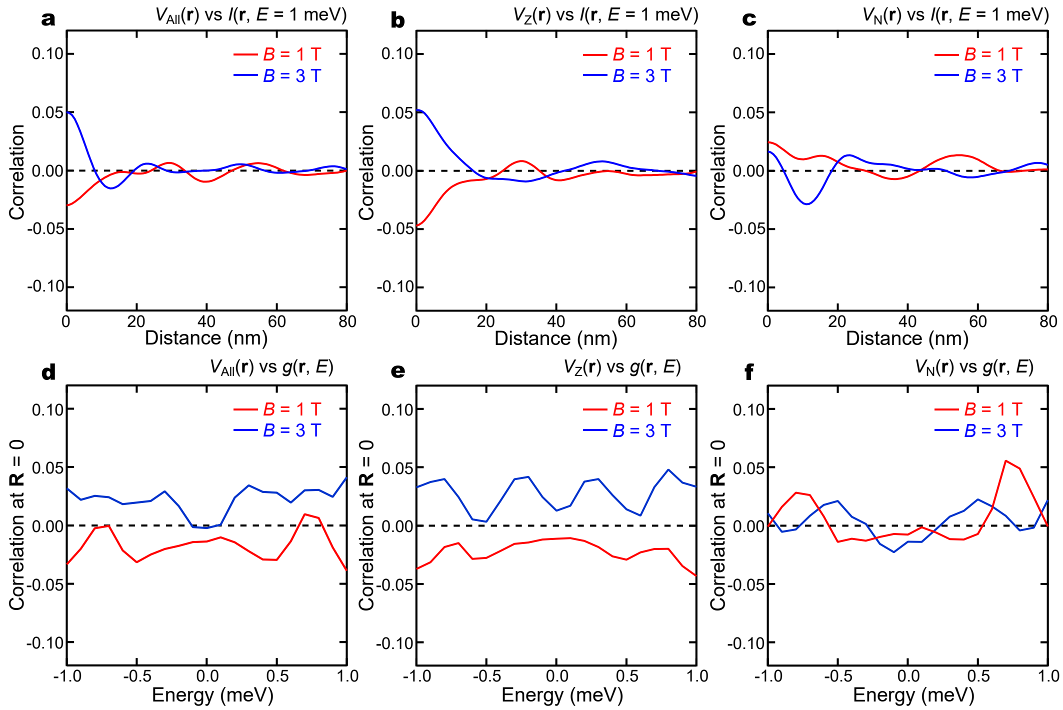

FIG. S7. **Correlation between the vortices and defects. a-c**, Azimuthally-averaged cross-correlation functions between the defect image $I(\mathbf{r}, E = 1\text{ meV})$ and the images representing all the vortices, the vortices with the ZVBS, and the vortices without the ZVBS, respectively. **d-f**, Energy dependence of the cross-correlation functions at $R = 0$ between $g(\mathbf{r}, E)$ and the images representing all the vortices, the vortices with the ZVBS, and the vortices without the ZVBS, respectively. Red and blue lines denote the results at $B = 1$ T and 3 T, respectively.

Correlations between vortices and local superconducting gap

Finally, we investigated the spatial correlation between vortices and the local superconducting gap $\Delta(\mathbf{r})$. Figure S8**a-c** shows the azimuthally-averaged $C[V_{\rm All}(\mathbf{r}); \Delta(\mathbf{r}), R]$, $C[V_{\rm Z}(\mathbf{r}); \Delta(\mathbf{r}), R]$, and $C[V_{\rm N}(\mathbf{r}); \Delta(\mathbf{r}), R]$, respectively. The absolute values never exceed 0.1 in all the cases. This suggests that the ZVBS is not related to the local superconducting-gap size.

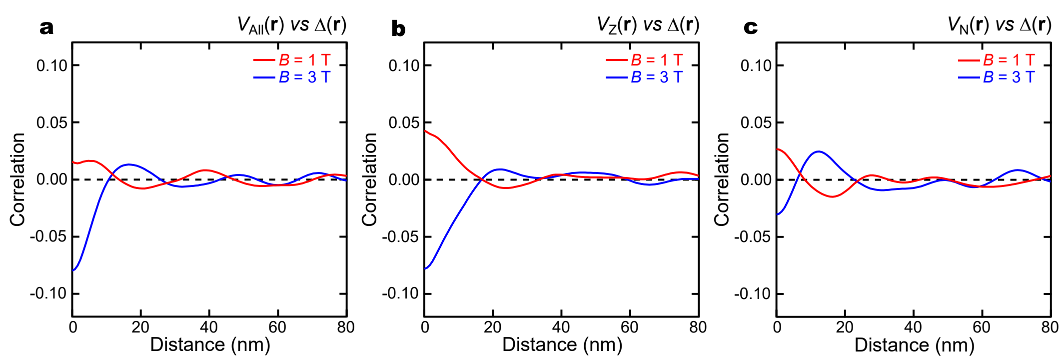

FIG. S8. **Correlation between the vortices and local superconducting gap. a-c**, Azimuthally-averaged cross-correlation functions between the superconducting-gap map $\Delta(\mathbf{r})$ and, all the vortices, the vortices with the ZVBS, and the vortices without the ZVBS, respectively. Red and blue lines denote the results at $B = 1$ T and 3 T, respectively.

VI. TUNNELING SPECTRA AT THE SAME LOCATIONS IN DIFFERENT MAGNETIC FIELDS

We found that four vortices reside at the same locations at $B = 1$ T and at 3 T. This provides us with an opportunity to investigate whether the ZVBS is governed by the local environment, or surrounding vortices and/or magnetic field itself play a role. Tunneling spectra taken at centers of such vortices are shown in Figure S9 for both 1 T and 3 T. Spectra are obviously different between 1 T and 3 T. In particular, at the position #2 defined in Fig. S9**a**,**b**, the ZVBS is absent at 1 T but is visible at 3 T. The opposite situation happens at #3. The finite-energy peaks also changes between 1 T and 3 T. These observations clearly indicate that the ZVBS is not governed by the local environment.

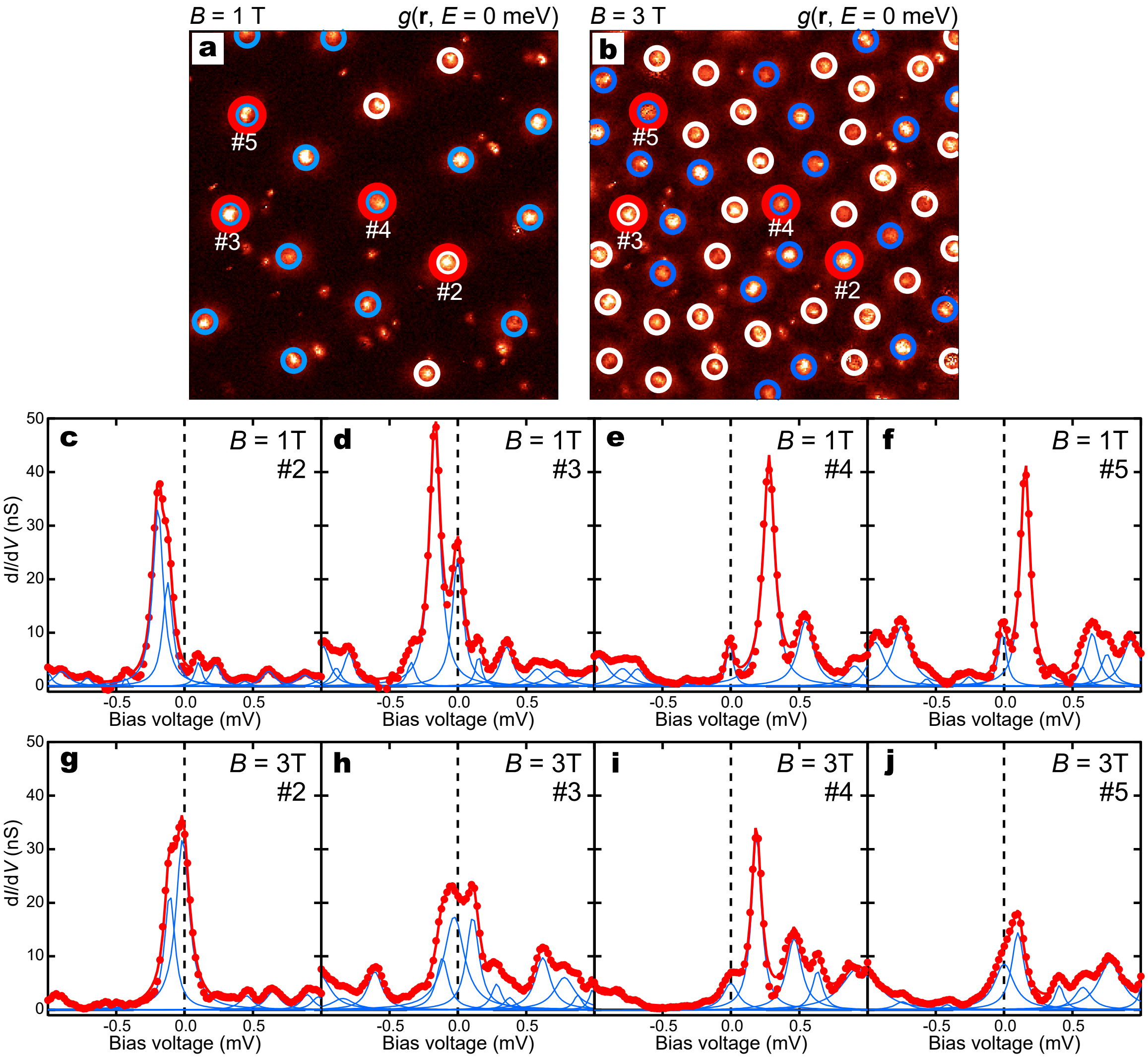

FIG. S9. **Comparison of the spectra at the same locations in different magnetic fields.** **a**,**b**, Maps of $g(\mathbf{r}, E = 0$ meV) at $B = 1$ T and 3 T, respectively, showing vortices. Blue and white circles represent the locations of vortices with and without the ZVBS. The vortices located at the same position between 1 and 3 T are indicated in red and their positions are labeled as #2 $\sim$ #5. **c**-**f**, Tunneling spectra at $B = 1$ T at the centers of vortices #2 $\sim$ #5, respectively. **g**-**j**, Tunneling spectra at $B = 3$ T at the centers of vortices #2 $\sim$ #5, respectively.

VII. CHECKING REPRODUCIBILITY IN A DIFFERENT FOV

To confirm the reproducibility of the diminishing ZVBS at higher B, we repeated the same experiments and analyses in a different FOV that is about 600 nm away from the original FOV investigated in the main text. As shown in Fig. S10, vortex lattices without orientational correlation, and the decreasing fraction of vortices with the ZVBS with increasing B are reproduced.

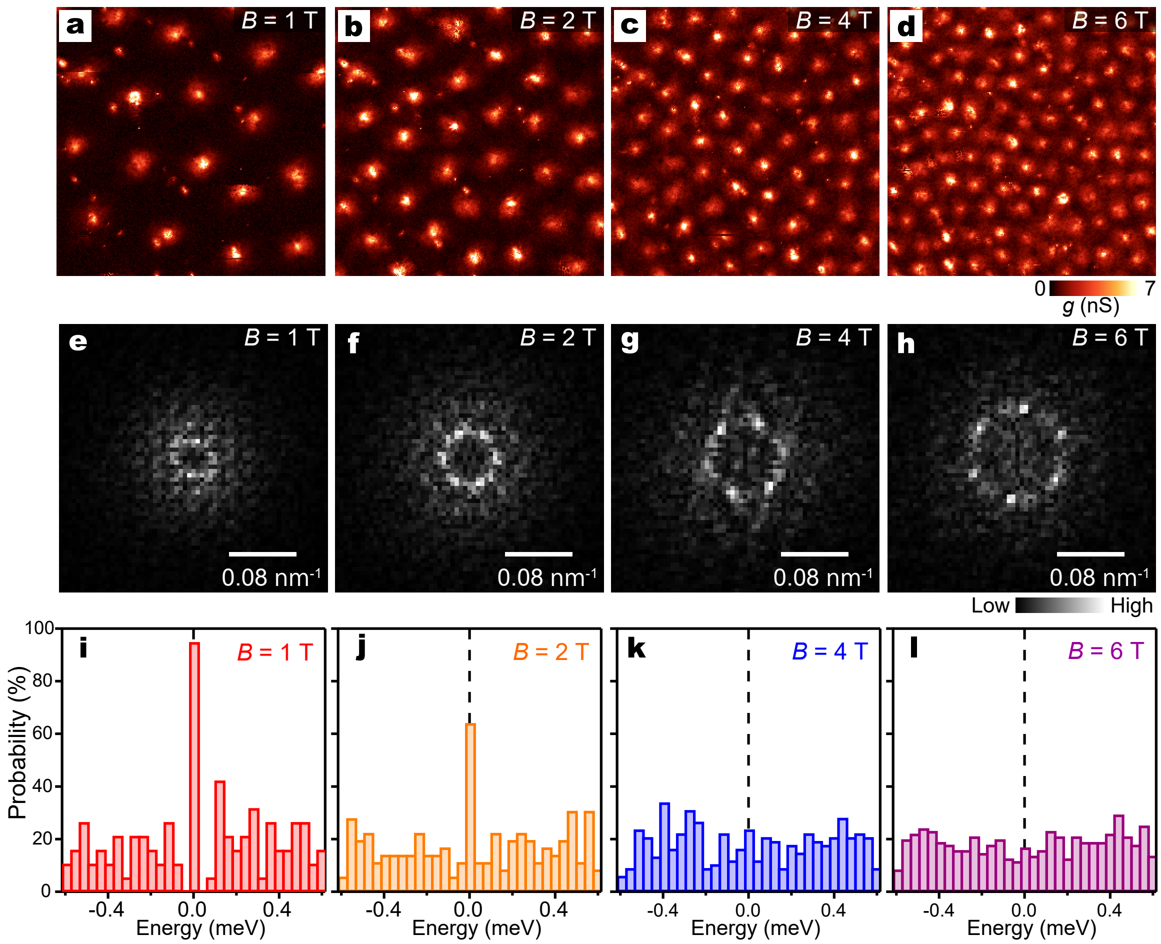

FIG. S10. **Vortices and the appearance probability of the ZVBS in a different FOV. a-d**, Maps of $g(\mathbf{r}, E = 0$ meV) in a 187 nm × 187 nm FOV at $B = 1$, 2, 4, and 6 T, respectively. These images were taken with the same experimental conditions as Fig. 4**a-e**, except the FOV. **e-h**, Fourier transformed images of **a-d**, respectively. **i-l** Histograms of the appearance probability of the peaks at given energies. All the imaged vortices in the FOV were used for the analyses at all B.

[S1] Hanaguri, T., *et al.* Two distinct superconducting pairing states divided by the nematic end point in $FeSe_{1-x}S_x$. *Sci. Adv.* **4,** eaar6419 (2018).
[S2] Singh, U. R., *et al.* Evidence for orbital order and its relation to superconductivity in $FeSe_{0.4}Te_{0.6}$. *Sci. Adv.* **1,** e1500206 (2015).
[S3] He, X., *et al.* Nanoscale chemical phase separation in $FeTe_{0.55}Se_{0.45}$ as seen via scanning tunneling spectroscopy. *Phys. Rev. B* **83,** 220502 (2011).
[S4] Lawler M. J., *et al.* Intra-unit-cell electronic nematicity of the high-Tc copper-oxide pseudogap states. *Nature* **466,** 347-351 (2010).
[S5] Wang Z., *et al.* Topological nature of the $FeSe_{0.5}Te_{0.5}$ superconductor. *Phys. Rev. B* **92,** 115119 (2015).
[S6] Wu X., *et al.* Topological characters in $Fe(Te_{1-x}Se_x)$ thin films. *Phys. Rev. B* **93,** 115129 (2016).
[S7] Xu G., *et al.* Topological Superconductivity on the Surface of Fe-Based Superconductors. *Phys. Rev. Lett.* **117,** 047001 (2016).
[S8] Zhang, P. *et al.* Observation of topological superconductivity on the surface of an iron-based superconductor. *Science* **360,** 182-186 (2018).